










Article

Synthesis and Study of Oxide Semiconductor Nanoheterostructures in SiO₂/Si Track Template

Alma Dauletbekova ^{1,*}, Diana Junisbekova ¹, Zein Baimukhanov ¹, Aivaras Kareiva ², Anatoli I. Popov ^{3,4}, Alexander Platonenko ³, Abdirash Akilbekov ^{1,*}, Ainash Abdrakhmetova ¹, Gulnara Aralbayeva ¹, Zhanyngul Koishybayeva ¹ and Jonibek Khamdamov ⁵

¹ Department of Technical Physics, L.N. Gumilyov Eurasian National University, Satpayev Str. 2, Astana 010008, Kazakhstan; diana911115@gmail.com (D.J.); zeinb77@mail.ru (Z.B.); abdrakhmetova_aa@enu.kz (A.A.); agm_555@mail.ru (G.A.); zhanyngul.k@gmail.com (Z.K.)

² Faculty of Chemistry and Geosciences, University of Vilnius, Naugarduko Str. 24, LT-03225 Vilnius, Lithuania; aivaras.kareiva@chgf.vu.lt

³ Institute of Solid-State Physics, University of Latvia, Kengaraga 8, LV-1063 Riga, Latvia; anatoli.popov@cfi.lu.lv (A.I.P.); alexander.platonenko@gmail.com (A.P.)

⁴ Institute of Physics, University of Tartu, W. Ostwald Str. 1, 50411 Tartu, Estonia

⁵ Institute of Semiconductor Physics and Microelectronics, National University of Uzbekistan, Yangi Almazar Str., 20, Tashkent 10005, Uzbekistan; jonibek.uzmu@gmail.com

* Correspondence: alma_dauletbek@mail.ru (A.D.); akilbekov_at@enu.kz (A.A.)

Abstract: In this study, chemical deposition was used to synthesize structures of Ga₂O₃-NW/SiO₂/Si (NW—nanowire) at 348 K and SnO₂-NW/SiO₂/Si at 323 K in track templates SiO₂/Si (either n- or p-type). The resulting crystalline nanowires were δ -Ga₂O₃ and orthorhombic SnO₂. Computer modeling of the delta phase of gallium oxide yielded a lattice parameter of $a = 9.287 \text{ \AA}$, which closely matched the experimental range of $9.83\text{--}10.03 \text{ \AA}$. The bandgap is indirect with an $E_g = 5.5 \text{ eV}$. The photoluminescence spectra of both nanostructures exhibited a complex band when excited by light with $\lambda = 5.16 \text{ eV}$, dominated by luminescence from vacancy-type defects. The current–voltage characteristics of δ -Ga₂O₃ NW/SiO₂/Si-p showed one-way conductivity. This structure could be advantageous in devices where a reverse current is undesirable. The p-n junction with a complex structure was formed. This junction consists of a polycrystalline nanowire base exhibiting n-type conductivity and a monocrystalline Si substrate with p-type conductivity. The I–V characteristics of SnO₂-NW/SiO₂/Si suggested near-metallic conductivity due to the presence of metallic tin.

Keywords: nanoheterostructure; oxide semiconductors; track template SiO₂/Si; δ -Ga₂O₃; orthorhombic SnO₂; photoluminescence; I–V characteristic



Citation: Dauletbekova, A.; Junisbekova, D.; Baimukhanov, Z.; Kareiva, A.; Popov, A.I.; Platonenko, A.; Akilbekov, A.; Abdrakhmetova, A.; Aralbayeva, G.; Koishybayeva, Z.; et al. Synthesis and Study of Oxide Semiconductor Nanoheterostructures in SiO₂/Si Track Template. *Crystals* **2024**, *14*, 1087. <https://doi.org/10.3390/cryst14121087>

Academic Editor: Dmitri Donetski

Received: 29 September 2024

Revised: 3 December 2024

Accepted: 11 December 2024

Published: 18 December 2024



Copyright: © 2024 by the authors. Licensee MDPI, Basel, Switzerland. This article is an open access article distributed under the terms and conditions of the Creative Commons Attribution (CC BY) license (<https://creativecommons.org/licenses/by/4.0/>).

1. Introduction

One of the current trends in materials science is the development of new materials and technologies for oxide photonics, sensors, and optoelectronics. In parallel, the trend towards miniaturizing device sizes continues. Optoelectronic devices based on one-dimensional nanowires (1D NWs) are being developed, including examples such as emitters, detectors, and transistors. These research areas offer promising opportunities for improving performance and reducing power consumption in the fields of nanotechnology and microelectronics [1–7].

A notable representative of oxide semiconductors is gallium oxide (Ga₂O₃), which has garnered significant attention due to its excellent chemical and thermal stability (up to 1400 °C) [8]. It is a wide-bandgap semiconductor with an energy bandgap of $E_g = 4.9 \text{ eV}$ at room temperature [9,10] and exhibits high transparency across a wavelength range from ultraviolet to visible light. Due to these unique properties, Ga₂O₃ is widely used in UV optical emitters [11,12], transparent conductors [13], and transparent electronic

devices [14]. Its thermal stability enables applications in high-temperature gas sensors [15], and Ga_2O_3 is also used in field-effect transistors [16,17] and solar photodetectors [18–20]. In recent years, the development of nano-functional devices based on low-dimensional Ga_2O_3 nanostructures has been reported, such as nanowire field-effect transistors [21,22] and nanophotonic switches [23].

Depending on the synthesis conditions, gallium oxide can form several different crystalline structures, such as α -, β -, γ -, δ -, and ϵ -phases. The β -form is the most common and well-studied polymorph of gallium oxide. Monoclinic β - Ga_2O_3 is considered the only stable phase over the entire temperature range up to its melting point, while the other phases are metastable and typically convert into β - Ga_2O_3 at high temperatures [24].

Various Ga_2O_3 nanostructures are synthesized through different methods such as thermal evaporation, arc discharge, hydrothermal techniques, chemical vapor deposition (CVD), and metal–organic chemical vapor deposition (MOCVD) [25–29]. Many researchers have invested significant efforts into developing Ga_2O_3 NW devices for future applications [23,30,31]. However, the controlled synthesis of Ga_2O_3 -NW with desired physical, chemical, and optical properties remains a challenging task.

Tin dioxide (SnO_2), an n-type oxide semiconductor, is widely studied due to its valuable properties such as a large bandgap ($E_g = 3.6$ eV at room temperature), thermal and chemical stability, environmental friendliness, and low cost. This material has been used to create various active nanostructures and shows promising results across a broad range of applications including gas sensors, lithium batteries, photocatalysis, photoluminescence, and more.

An interesting aspect of SnO_2 NW synthesis is the potential to “tune” its physical properties by carefully controlling the morphology of the nanomaterial, enabling the development of devices that meet specific technological challenges [32]. However, relatively few studies have focused on the UV-sensing properties of SnO_2 NWs [33–37], which are important not only for understanding light detection mechanisms but also for the development of high-performance nanodevices for future optoelectronic circuits, imaging techniques, and communication systems.

Solution-based deposition methods offer a highly efficient and viable approach for synthesizing nanomaterials from semiconductor oxides. These methods often require templates and additives to direct the material’s growth towards the desired morphology. SiO_2/Si templates, for instance, can be prepared by irradiating SiO_2/Si structures with swift heavy ions, followed by track etching in selective etchants to create nanopores. These pores can then be filled with various materials. Template-assisted synthesis enables the formation of unique compounds that typically require specific conditions to be produced [38–44].

This method has demonstrated great potential in creating novel structures and functional materials for a wide range of applications, including photonics, sensors, and nano-electronics [45–49].

The goal of our research is to synthesize gallium oxide (Ga_2O_3) and tin dioxide (SnO_2) nanowires using template-assisted synthesis, which is based on chemical deposition into nanoporous SiO_2/Si structures.

2. Materials and Methods

2.1. Formation and Characterization of a Track Template

The studies used Si (100) wafers in the form of disks with a diameter of 10 cm and a thickness of 500 μm . For n-type Si, a phosphorus impurity with a concentration of 1 ppm was used, and for p-type Si, a boron impurity of 1 ppm was used.

An oxide layer with a thickness of approximately 530 nm was thermally grown on a silicon wafer (Si (100)) at 900 °C in a humid atmosphere.

The prepared a- SiO_2/Si disks were irradiated with 200 MeV Xe ions at fluences of 10^7 – 10^8 ions/ cm^2 using the DC-60 accelerator (Astana, Kazakhstan). In the selected fluence range, no track overlap was observed, allowing for a uniform distribution of tracks across the surface and a low background of radiation-induced defects [50].

Figure 1 illustrates the calculations of electronic energy loss (S_e), nuclear energy loss (S_n), and the ion range of 200 MeV xenon in a-SiO₂/Si, obtained using the SRIM code [51]. These parameters are crucial for understanding how energetic ions interact with the material, affecting its structural and electronic properties during irradiation. The graph provides insights into the deposition of energy into the material, which influences defect formation and nanostructure synthesis processes.

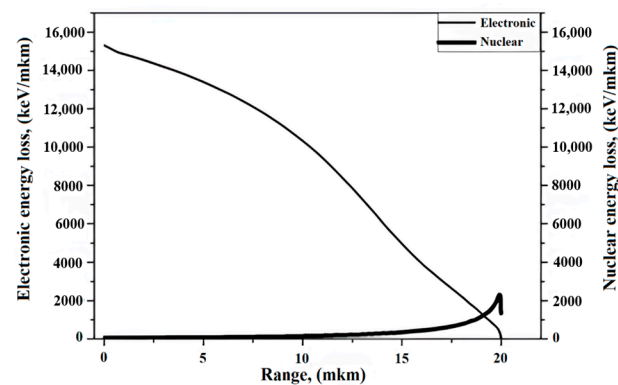


Figure 1. Electronic and nuclear energy losses for the 200 MeV Xe ion in the SiO₂/Si structure calculated by the SRIM code.

According to the SRIM code, the electronic energy loss of Xe ions in the SiO₂ layer is approximately two orders of magnitude higher than the nuclear energy losses. The electronic energy loss in the SiO₂ layer remains nearly constant at $\approx 15.2 \text{ keV nm}^{-1}$, which significantly exceeds the threshold value (4 keV nm^{-1}) required for the formation of latent tracks in the SiO₂ matrix [52]. When ionization energy losses surpass 4 keV nm^{-1} , the latent tracks can be etched to form pores with uniform shape and narrow size distribution, achieving an etching efficiency of nearly 100%. This behavior is critical for applications involving nanostructure fabrication through ion irradiation.

After oxidation, the wafers were cut into samples of $10 \times 10 \text{ mm}^2$. The samples were treated with a 4% aqueous solution of hydrofluoric acid (HF) for 5–7 min at room temperature to form nanopores (Figure 2). This etching process selectively removes the irradiated regions, creating pores with a controlled shape and size. HF treatment is commonly used to etch SiO₂ due to its ability to dissolve silica, and the duration of exposure allows precise control over the pore structure. This method is essential for creating nanostructure templates for further material deposition.

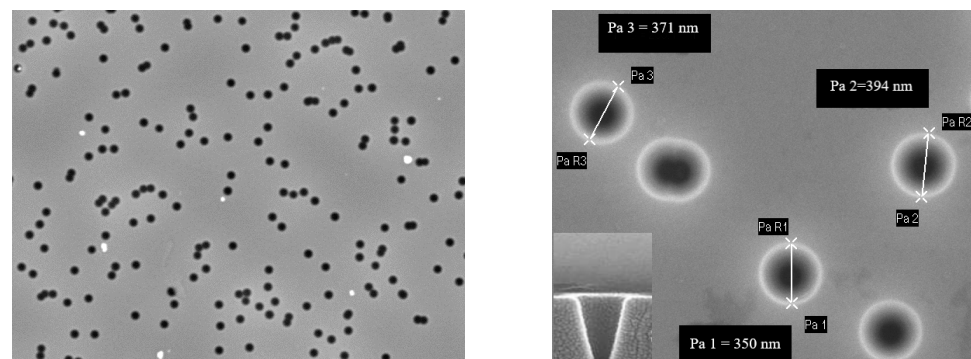


Figure 2. SEM image of surface of track template a-SiO₂/Si.

2.2. Methods for Filling Nanopores of Template

The chemical deposition (CD) of Ga₂O₃ nanowires into n- and p-type templates was carried out using a chloride solution for varying durations (from 15 to 30 min). The

CD solution was prepared by dissolving pure Ga_2O_3 powder (10 g/L) in concentrated hydrochloric acid (20 mL). Deionized water was then added in the required amount. The solution was continuously stirred and heated to 75 °C using a magnetic stirrer until a clear solution was obtained. To adjust the pH of the solution to a range of 2 to 6, a buffer solution (15 mL of ammonia) was added. This process helps control the conditions for Ga_2O_3 nanowire growth within the template pores.

The prepared SiO_2/Si matrices were immersed in the solution, and the chemical deposition process was carried out at 348 K for a specified period. For the synthesis of tin dioxide (SnO_2) nanowires via chemical deposition, a solution consisting of 0.67 g SnSO_4 , 4 g $\text{CH}_4\text{N}_2\text{S}$, and 2 mL H_2SO_4 was used. $\text{CH}_4\text{N}_2\text{S}$ was dissolved in deionized water, while SnSO_4 was dissolved in a minimal amount of concentrated sulfuric acid. The two solutions were then combined, and the pH was adjusted to a range of 2 to 4. The chemical deposition of SnO_2 nanowires was carried out at 323 K.

2.3. Study of Structural, Optical, Electrophysical Properties

A scanning electron microscope (SEM) was used to monitor the surface condition of the samples. To determine the crystallographic structure of the material, X-ray diffraction (XRD) analysis was performed. The structure of the precipitates was examined using a D8 ADVANCE ECO X-ray diffractometer equipped with a Cu-anode X-ray tube. Data were collected in the 2θ angular range of 30° to 110° with a step size of 0.01°. The phases and crystalline structures were identified using Bruker AXS DIFFRAC software DiffracEVA v.4.2.

For studying the electrical properties of the nanowire arrays, a setup was used (Figure 3), consisting of an HP 66312A current source and an Agilent 34401A multimeter, Keysight, Santa Rosa, CA, USA. The current–voltage characteristics (CVCs) were measured from an array of filled nanowires with a total surface area of 0.3 cm². The schematic of the experimental setup is shown in Figure 3.

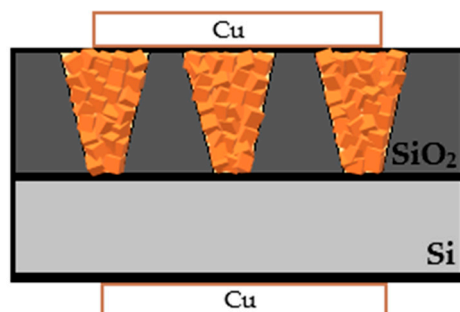


Figure 3. Current–voltage characteristic (CVC) measurement circuit.

The photoluminescence (PL) spectra of the samples were measured using a CM2203 fluorescent spectrophotometer (Solar, Belarus). The samples were excited by light with a wavelength of 240 nm, emitted from a xenon lamp. The PL spectra were recorded over the wavelength range of 300 nm to 800 nm at room temperature.

3. Results and Discussion

3.1. Experimental and Theoretical Study of $\text{Ga}_2\text{O}_3\text{-NW}/\text{SiO}_2/\text{Si}$ and $\text{SnO}_2\text{-NW}/\text{SiO}_2/\text{Si}$ Structures

3.1.1. $\text{Ga}_2\text{O}_3\text{-NW}/\text{SiO}_2/\text{Si}$

In Figure 4, the SEM images display the surface of the samples after etching and deposition with gallium oxide. The SEM images allow for detailed visualization of the nanostructures formed on the SiO_2/Si template.

Analysis of the SEM images revealed that the nanopores in the investigated samples had a filling degree of 32%, with an average nanopore diameter of 215 nm. The results of the X-ray structural analysis are presented in Figures 5 and 6, as well as in Tables 1 and 2,

for samples after chemical deposition, which differ based on the conductivity type of the Si substrate.

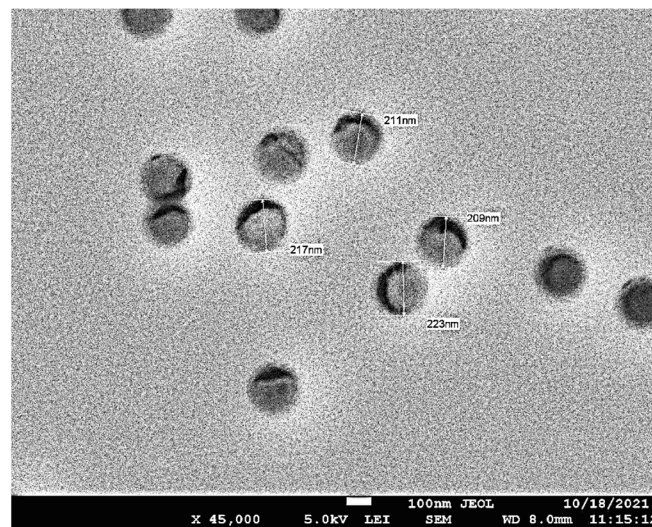


Figure 4. SEM image of the surface of the p-type template after CD of Ga_2O_3 ($t = 15$ min), at $T = 348$ K.

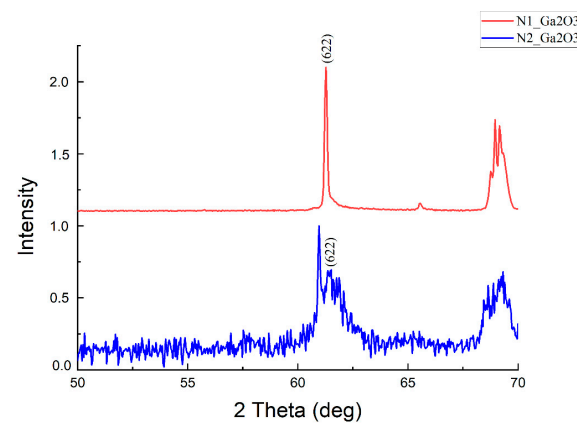


Figure 5. X-ray diffractograms of $\text{SiO}_2/\text{Si-p}$ templates after chemical deposition (CD) are as follows: (N1) with a deposition time of $t = 15$ min at $T = 348$ K (75°C); (N2) with a deposition time of $t = 30$ min at $T = 348$ K.

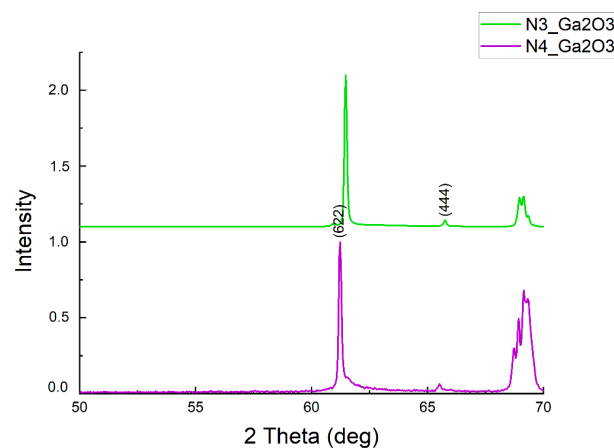


Figure 6. X-ray diffractograms of $\text{SiO}_2/\text{Si-n}$ type templates after chemical deposition (CD) at $T = 348$ K (75°C) were obtained for two different deposition durations: (N3) for a deposition time of 15 min; (N4) for a deposition time of 30 min.

Table 1. Crystallographic characteristics of Ga₂O₃-NW/SiO₂/Si (p-type) based on X-ray diffraction analysis.

Phase Name	Structure Type	Space Group	(hkl)	2 θ	d, Å	Cell Parameters, Å	Volume, Å ³	Size of Crystallite, Å	Density, g/cm ³
N1									
Ga ₂ O ₃	Cubic	206: Ia-3	(622)	61.271 (6)	1.51165 (13)	a = 10.027141; $\alpha = \beta = \gamma = 90$	1008.164311	100.0	4.940
N2									
Ga ₂ O ₃	Cubic	206: Ia-3	(622)	61.33 (3)	1.6377	a = 10.018919; $\alpha = \beta = \gamma = 90$	1005.686444	100.0	4.952

Table 2. Crystallographic characteristics of Ga₂O₃-NW/SiO₂/Si substrates (n-type) based on X-ray diffraction analysis.

Phase Name	Structure Type	Space Group	(hkl)	2 θ	d, Å	Cell Parameters, Å	Volume, Å ³	Size of Crystallite, Å	Density, g/cm ³
N3									
Ga ₂ O ₃	Cubic	206: Ia-3	(444)	65.76 (9)	1.4190 (17)	a = 9.830884; $\alpha = \beta = \gamma = 90$	950.118314		5.242
Ga ₂ O ₃	Hexagonal	167: R-3c	(116)	55.98 (8)	1.641 (2)	a = 4.933100; b = 4.933100; c = 13.422600 $\alpha = \beta = 90$; $\gamma = 120$	282.883201	100.0	6.602
N4									
Ga ₂ O ₃	Cubic	206: Ia-3	(622)	61.226 (10)	1.5126 (2)	a = 10.033777; $\alpha = \beta = \gamma = 90$	1010.167374	100.0	4.930

Increasing the deposition time in SiO₂/Si-p leads to a decrease in the XRD signal, which is most likely due to a decrease in the number of crystallites created, caused by solution evaporation because the synthesis proceeds at a sufficiently high temperature at T = 348 K (75 °C). This forms delta gallium oxide with smaller lattice parameters of 10.018919 Å, and with decreases in density and volume. The same effect of reducing the intensity of the XRD signal is also observed in Figure 6. The bands with 2 θ = 68 are associated with silicon.

As the deposition time increases, the hexagonal phase of Ga₂O₃ disappears, indicating a transformation into a more stable structure. Gallium oxide, which is classified as a transparent conducting oxide (TCO), can exist in multiple polymorphic forms, each with its unique crystallographic structure and gallium ion coordination environment. The known polymorphs include α -, β -, γ -, δ -, and ϵ -Ga₂O₃, with a transitional ζ -Ga₂O₃ phase also reported in the literature. These polymorphs differ not only in their crystal space groups but also in the coordination numbers of gallium ions.

In our research, we obtained the δ -Ga₂O₃ structure, which was first studied in the work of [53] and computationally analyzed in reference [54]. This phase represents one of the less common polymorphs, and our findings contribute to a better understanding of its formation and properties under different synthesis conditions.

The crystalline structure of δ -Ga₂O₃ belongs to the 206: Ia-3 space group and has a body-centered cubic structure with a lattice parameter of a = 10.00 Å according to experimental data [53], and a = 9.401 Å based on theoretical calculations [54]. This structure was obtained for four samples synthesized through chemical deposition at a constant temperature of 75 °C, using the same solution but with variations in the Si substrate conductivity type and deposition time (Tables 1 and 2).

For samples N1 and N2, which used a p-type Si substrate, the cubic phase of Ga₂O₃ formed in both cases. As the deposition time increased from 15 to 30 min, the lattice param-

eter slightly decreased from 10.027141 Å to 10.018919 Å, with crystallite sizes remaining consistent at 100 Å.

In contrast, for samples N3 and N4, which used an n-type Si substrate, the same cubic Ga_2O_3 phase formed after 15 min of deposition. However, extending the deposition time to 30 min (sample N4) led to the emergence of a hexagonal phase ($\epsilon\text{-Ga}_2\text{O}_3$) alongside the cubic phase. The lattice parameter of the cubic phase decreased to 9.830884 Å, while in the purely cubic phase of sample N3, it was 10.033777 Å.

The similarity between our chemical deposition method and the hydrothermal process used in the study by [53] may lie in the formation of a “Gallia–water complex”, which contributes to the growth of $\delta\text{-Ga}_2\text{O}_3$. In the hydrothermal process, gallium gel prepared from an aqueous nitrate solution was subjected to specific pressure and temperature conditions (0–50 °C) to form this complex, which facilitated the crystallization of $\delta\text{-Ga}_2\text{O}_3$. Similarly, in our CD method, a comparable “Gallia–water complex” likely forms at 75 °C, leading to the growth of the $\delta\text{-Ga}_2\text{O}_3\text{-NW/SiO}_2\text{/Si}$ structure.

3.1.2. Computer Modeling of the Crystalline and Electronic Structure of $\delta\text{-Ga}_2\text{O}_3$

Computational modeling of the delta phase of gallium oxide was performed using an ab initio CRYSTAL23 [55] code within the approximation of Linear Combination of Atomic Orbitals (LCAO), using hybrid PBE0 exchange–correlation functional [56,57] and POB-TZVP-rev2 basis sets [58].

The delta phase of Ga_2O_3 has a cubic bixbyite structure (space group 206), with two inequivalent gallium ions occupying 8d and 24d Wyckoff positions, and oxygens occupying 48e positions. This results in 40 atoms in the primitive cell, and 80 atoms in the conventional crystallographic cell (Figure 7). The optimized cell parameter is 9.29 Å with Ga–O bond lengths ranging from 1.99 to 2.04 Å. The calculated value is $a = 9.287$ Å, which is close to our experimental data lying in the range of 9.83–10.03 Å.

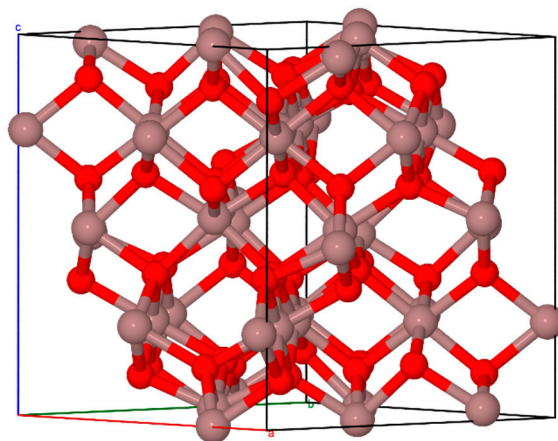


Figure 7. Crystallographic cell of $\delta\text{-Ga}_2\text{O}_3$ consisting of 80 atoms. Gallium atoms are shown in brown, and oxygen is shown in red.

The electronic structure of $\delta\text{-Ga}_2\text{O}_3$ is shown in Figure 8. Similar to other Ga_2O_3 phases, the calculated bandgap is indirect and is about 5.5 eV. However, the difference between direct and indirect transitions is less than 0.1 eV and the top of the valence band is relatively flat. While the bottom of the conduction band is in the Gamma point, all other high-symmetry points of the Brillouin zone are higher by ~2 eV.

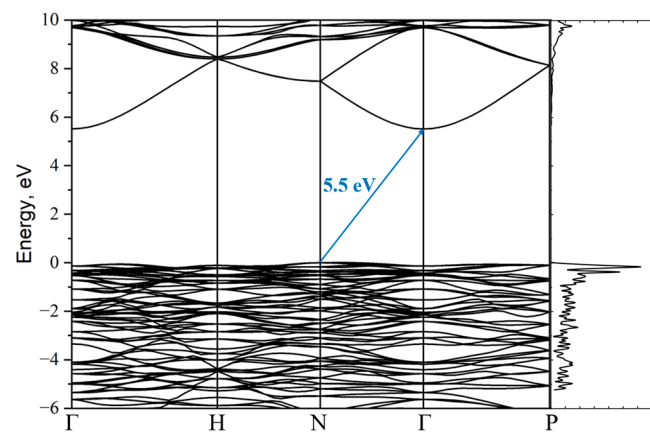


Figure 8. Band structure and density of states of δ -Ga₂O₃.

3.1.3. SnO₂-NW/SiO₂/Si

Figure 9 shows the SEM image of the template surface after chemical deposition (CD).

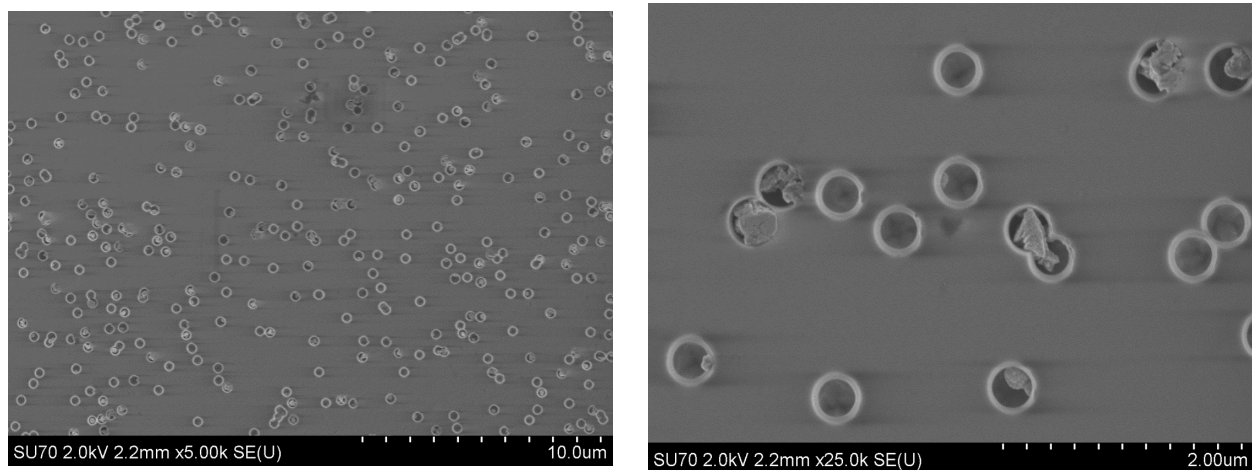


Figure 9. The SEM image of the SiO₂/Si-n template surface after SnO₂ CD for 20 min at a temperature of 323 K.

As seen in Figure 9, the nanowires clearly filled the nanopores after 20 min of chemical deposition. Analysis of the SEM images revealed that the diameter of the nanopores varied between 350 nm and 430 nm, with an overall filling degree of 80%.

According to the X-ray diffraction analysis (XRD) shown in Figure 10, the CD process led to the formation of SnO₂ nanowires with an orthorhombic structure belonging to the symmetry space group Pnnm (58). Additionally, a phase of tin (Sn) with a tetragonal structure and symmetry space group I4/mmm (139) was identified. The detailed results of the X-ray structural analysis for this sample are provided in Table 3, indicating the crystalline phases and structural parameters, confirming the successful synthesis of SnO₂ nanowires and the presence of metallic tin within the template.

The X-ray diffraction analysis indicates that the ratio of the Sn phase to the SnO₂ phase is approximately 22% to 78%, respectively. It is noteworthy that in our previous study [59], orthorhombic SnO₂ (O) was obtained via electrochemical deposition, and the lattice parameters differed significantly. This discrepancy is likely due to the formation of metallic tin (Sn) in the current study. It appears there might be a deficiency of oxygen ions in the nanopores, which is further supported by the photoluminescence (PL) results, where a dominance of defect-related luminescence was observed. This suggests that oxygen

deficiency plays a crucial role in influencing the structural and optical properties of the synthesized SnO₂ nanowires.

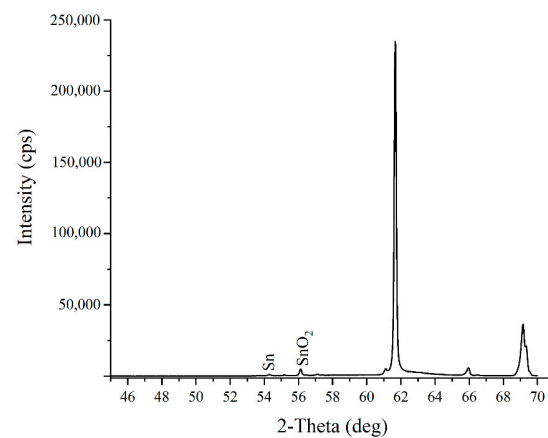


Figure 10. X-ray diffractogram of SnO₂ samples obtained by chemical deposition for 20 min at a temperature of 323 K.

Table 3. Crystallographic parameters of SnO₂-NW/SiO₂/Si-n track template based on XRD analysis.

Phase Name	Structure Type	Space Group	(hkl)	2θ	d, Å	Cell Parameters, Å	Volume, Å ³	Size of Crystallite, Å	Density, g/cm ³
Sn	Tetragonal	139: I4/mmm	(002)	54.271	1.6889	A = 3.674736; b = 3.674736; c = 3.377628	45.610417	58.0	8.644
SnO ₂	Orthorhombic	58: Pnnm	(220)	56.113	1.6377	a = 4.655800; b = 4.599800; c = 3.151400	67.489592	58.71	7.416

3.2. Photoluminescence of δ -Ga₂O₃-NW/SiO₂/Si and SnO₂-NW/SiO₂/Si

Figure 11 shows the photoluminescence (PL) spectra at room temperature (RT) of δ -Ga₂O₃-NW/SiO₂/Si. The PL spectra were plotted considering the luminescence of the samples before deposition. The optical properties were studied in the spectral range from 3.8 eV to 2 eV with excitation light at $\lambda = 5.16$ eV. This excitation corresponds to the exciton band, considering the calculated bandgap of δ -Ga₂O₃ as $E_g = 5.5$ eV from Section 3.1.2.

Due to its wide bandgap nature, β -Ga₂O₃ can emit light from defect states over a broad spectral range from infrared (IR) to ultraviolet (UV) [9]. Previous studies have concluded that the fundamental bandgap of β -Ga₂O₃ is indirect with an $E_g = 4.84$ eV, while the direct bandgap at the Γ -point is only 0.04 eV higher, at 4.88 eV. This small energy difference and the weak nature of indirect transitions make β -Ga₂O₃ behave like a direct bandgap material, consistent with experimental sharp absorption starting at 4.9 eV [60–62].

Similarly, δ -Ga₂O₃ can also be considered a direct bandgap oxide semiconductor, justifying the comparison of the PL results of δ -Ga₂O₃ with the luminescence characteristics of β -Ga₂O₃. This direct bandgap property of δ -Ga₂O₃ makes it suitable for optoelectronic applications like β -Ga₂O₃.

The photoluminescence (PL) spectrum of β -Ga₂O₃ includes up to three distinct emission bands: an ultraviolet (UV) band (3.2–3.6 eV), a blue band (2.8–3.0 eV), and a green band (2.4 eV) [63–69].

The PL spectrum of δ -Ga₂O₃ (Figure 4 (N1)) reveals peaks at 2.2 eV, 2.5 eV, 2.78 eV, 3 eV, and 3.37 eV when decomposed into Gaussian components. The origin of the UV emission band, like that in β -Ga₂O₃, is likely associated with the recombination of self-trapped

excitons, meaning the recombination of electrons and holes from the lower level of oxygen vacancies to the valence band [70].

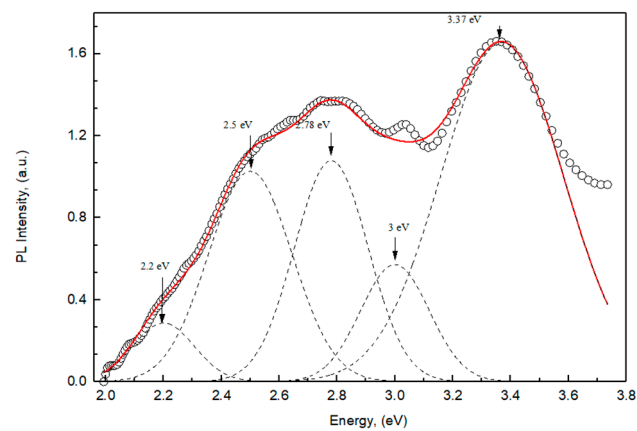


Figure 11. The PL spectrum of δ -Ga₂O₃-NW/SiO₂/Si obtained by (CD) at T = 348 K (75 °C) with a deposition time of 15 min. The excitation was carried out using light with a wavelength of $\lambda = 5.16$ eV. The hollow circle line represents the experimental curve, while the red line indicates the set of Gauss components.

The blue PL peaks at 2.5 eV and 2.78 eV, much like in β -Ga₂O₃, are probably due to transitions from donor levels formed by oxygen vacancies to acceptor levels formed by gallium vacancies and defect clusters, such as a pair of gallium and oxygen vacancies $v_{Ga} - v_O$ ([9,67]. The PL band with a maximum peak at 2.2 eV may result from the presence of silicon impurities [65]. Additionally, according to some sources [71,72], green luminescence can occur when excitons are self-trapped due to electron–lattice interactions or when they interact with impurities, defects, or vacancies.

The dominant defects in the δ -Ga₂O₃ structure are vacancy-type defects. It should be noted that the PL was very weak for samples N2, N3, and N4. For sample N2, this might be due to the formation of an additional hexagonal phase, while for samples N3 and N4, the weak PL could be attributed to the low filling of nanopores, which was observed for templates with a p-type Si substrate.

The PL spectrum of SnO₂-NW/SiO₂/Si was measured in the spectral range from 300 to 600 nm with excitation light at a wavelength of $\lambda = 240$ nm (5.17 eV). Figure 12 shows the decomposition of the PL spectrum into Gaussian components.

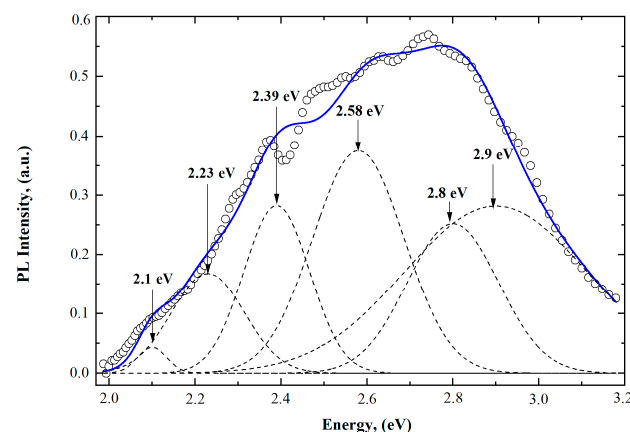


Figure 12. The PL spectrum of SnO₂-NW/SiO₂/Si, excited at a wavelength of $\lambda = 240$ nm. The hollow circle line represents the experimental curve, while the blue line indicates the set of Gauss components.

The photoluminescence (PL) spectra of $\text{SnO}_2\text{-NW/SiO}_2\text{/Si}$ synthesized through CD show differences when compared to those of $\text{SnO}_2\text{-NW/SiO}_2\text{/Si}$ obtained via the electrochemical method (ECD). The observed PL maxima were found at 2.9 eV (427 nm), 2.8 eV (442 nm), 2.58 eV (480 nm), 2.39 eV (518 nm), 2.23 eV (555 nm), and 2.1 eV (590 nm).

The luminescence centers responsible for the violet emission peak at 2.9 eV (427 nm) can be attributed to interstitial tin (Sn) or tin atoms with damaged bonds [73–77].

The blue light emission with a peak at 2.8 eV (442 nm) is likely caused by the transition from a triplet state to the ground state for oxygen vacancies v_{O}^0 [78]. Most oxygen vacancies are in a paramagnetic state v_{O}^+ , corresponding to the peak at 2.58 eV (480 nm) [75,79], while the peak at 2.39 eV (518 nm) is associated with a surface donor defect v_{O}^0 [80].

The peak at 2.23 eV (555 nm) might result from oxygen vacancies formed during the deposition process, as indicated in studies [81,82]. The emission at 2.1 eV (590 nm) corresponds to defect levels within the bandgap related to oxygen vacancies or interstitial Sn, like what has been observed in SnO_2 nanobelts synthesized by laser ablation [83] and SnO_2 nanorods grown using a solution-phase method [84].

It is well known that oxygen vacancies are the most common defect type and frequently act as luminescent centers. Indeed, the analysis of the PL spectrum indicates that the primary defects responsible for emission are oxygen vacancies rather than tin-related defects. A similar observation was made for $\delta\text{-Ga}_2\text{O}_3\text{-NW/SiO}_2\text{/Si}$, where oxygen vacancies also play a dominant role in luminescence properties.

3.3. Current–Voltage (I–V) Characteristics of $\delta\text{-Ga}_2\text{O}_3\text{-NW/SiO}_2\text{/Si}$ and $\text{SnO}_2\text{-NW/SiO}_2\text{/Si}$

The current–voltage characteristics (I–V or CVCs) were measured for $\delta\text{-Ga}_2\text{O}_3\text{-NW/SiO}_2\text{/Si-p}$ and $\text{SnO}_2\text{-NW/SiO}_2\text{/Si-n}$ samples, including the original untreated sample.

For the first sample (N1), a clear diode-like I–V characteristic (Figure 13) was observed, indicating n-type conductivity of $\delta\text{-Ga}_2\text{O}_3$ NWs. In contrast, the current values for the second sample (N2) were about seven times lower than those of the first sample. This decrease in current is probably due to the increase in the deposition time, which led to the solution's evaporation and a reduction in the number of crystallites. A decrease in the unit cell size was also observed. As a result, the boundary regions between crystallites increased, leading to the capture of more free charge carriers by the defects.

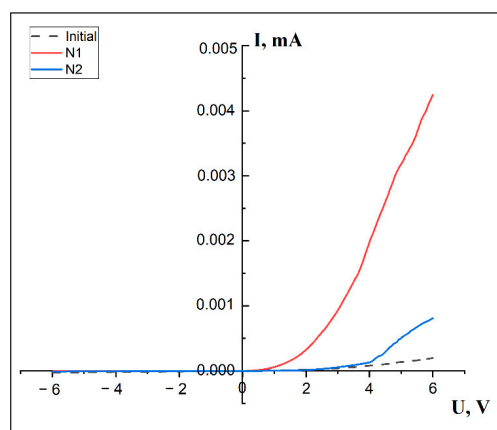


Figure 13. Current–voltage (I–V) characteristics of $\delta\text{-Ga}_2\text{O}_3\text{-NW/SiO}_2\text{/Si-p}$. The dashed curve represents the original, untreated sample. The red curve corresponds to the sample with $\delta\text{-Ga}_2\text{O}_3$ deposited for 15 min, a p-type Si substrate. The blue curve corresponds to the sample with $\delta\text{-Ga}_2\text{O}_3$ deposited for 30 min, a p-type Si substrate.

For sample N1, the $\delta\text{-Ga}_2\text{O}_3\text{-NW/SiO}_2\text{/Si-p}$ structure exhibits pronounced one-way conductivity. This structure is potentially feasible for use in devices where the reverse current is unacceptable or should be negligible. It should also be noted that a p–n junction

with a complex structure is created. It is the junction of a polycrystalline nanowire base with n-type conductivity and a single-crystalline Si substrate with p-type conductivity.

In polycrystalline nanowires, there are crystallites and intercrystallite boundaries. The presence of intercrystallite boundaries, the density of which is less than the electron density of the crystallite, leads to the formation of spatial volume charge on the boundary and, as a consequence, to the formation of multilayer potential barriers. The conductivity of polycrystalline nanowires depends on the size of potential barriers and the size of crystallites.

For the explanation of the conductivity of polycrystalline samples, diffusion and thermoemission models are used. The diffusion theory is applicable if the potential barrier width W is much larger than the free path length of carriers l . The thermoelectron emission model is applicable in the case where $l > W$. According to this model, only those carriers whose kinetic energy is greater than the barrier height can cross the boundary.

If we assume that, to each barrier (we believe that we have barriers of the same type), the average voltage V/m is applied (m is the number of obstacles between electrodes; V is the interelectrode voltage), then for the current–voltage characteristic, we can write the relation [85]

$$I = I_0 \exp [(-e (\varphi - V/m))/kT]$$

which determines the height of the potential barrier φ and the number of barriers m . This relation was used to analyze current transfer in polycrystalline gallium phosphite [86].

The value of I_0 is taken from the value of the conduction threshold voltage, which is 2 V. The number of barriers can be estimated from the formula $m = H/h_k$ where $H = 530$ nm is the height of the nanopore, and h_k is the linear size of the nanocrystallite, as we took the average value of crystal lattice parameters from Table 1 (10.03 Å). The barrier height was obtained as being equal to 0.06 eV.

It should be noted that internal defects do not significantly affect conductivity under ordinary conditions and begin to do so only with increasing temperature.

Figure 14 shows the I–V characteristics of the samples before and after SnO_2 deposition.

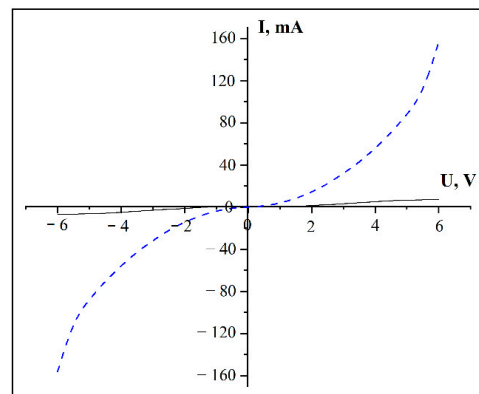


Figure 14. Current–voltage (I–V) characteristics of $\text{SnO}_2\text{-NW/SiO}_2\text{/Si-n}$. The solid curve represents the original, untreated sample. The dashed curve represents the sample after CD with a deposition time of 20 min.

It is evident that prior to deposition, conductivity was almost absent in both forward and reverse directions. After CD, the I–V characteristics exhibit a non-linear but nearly symmetrical shape in both directions, which is clearly related to the presence of metallic Sn. This behavior differs from the I–V characteristics of $\text{SnO}_2\text{-NW/SiO}_2\text{/Si-n}$ obtained by electrochemical deposition, as reported in [59], where the nanowires contained only the orthorhombic phase of SnO_2 .

4. Conclusions

In this study, crystalline nanowires of δ -Ga₂O₃ with the space group symmetry Ia-3 were synthesized in track templates SiO₂/Si (n- or p-type). The lattice parameters of the unit cell changed slightly depending on the deposition time, and the formation of an additional hexagonal phase of Ga₂O₃ was observed.

Computational modeling of the delta phase of gallium oxide was performed using the ab initio CRYSTAL23 [55] code, within the Linear Combination of Atomic Orbitals (LCAO) approximation, and utilizing the hybrid PBE0 exchange–correlation functional [57,58] and POB-TZVP-rev2 basis sets [58]. The calculated lattice parameter was $a = 9.287$ Å, which closely matches our experimental values, ranging between 9.83 Å and 10.03 Å.

The chemical deposition technique used in this research is quite similar to the hydrothermal method described in [53], suggesting the possible formation of a Gallia–water complex at 75 °C, which participates in the growth of δ -Ga₂O₃-NW/SiO₂/Si nanowires. This insight provides a better understanding of the synthesis process and the structural characteristics of the resulting nanowires.

The PL of δ -Ga₂O₃-NW/SiO₂/Si was excited with light at $\lambda = 5.16$ eV, resulting in a broad and complex PL band observed in the range from 3.8 eV to 2 eV. Decomposition into Gaussian components revealed the following PL peaks: 2.2 eV, 2.5 eV, 2.78 eV, 3 eV, and 3.37 eV. Comparing these with the PL spectra of β -Ga₂O₃, it was suggested that the UV emission band might be associated with the recombination of self-trapped excitons. The dominant defects are vacancy-type defects. Notably, samples N2, N3, and N4 exhibited very weak PL. For sample N2, this is likely due to the formation of an additional hexagonal phase, while for samples N3 and N4, the weak PL can be attributed to the low filling of nanopores, a common observation for templates with p-type substrates.

The investigation of the I–V characteristics showed that the N1 sample (the δ -Ga₂O₃-NW/SiO₂/Si-p structure) demonstrates significant one-way conductivity. This structure could be advantageous in devices where the reverse current is undesirable or should remain minimal. Additionally, it is important to note that a p–n junction with a complex structure has been formed. This junction consists of a polycrystalline nanowire base exhibiting n-type conductivity and a monocrystalline Si substrate with p-type conductivity.

The synthesis of SnO₂-NW/SiO₂/Si through chemical deposition into the track template at $T = 323$ K resulted in the formation of an orthorhombic SnO₂ phase, complemented by metallic tin (Sn). The PL spectrum of this structure also exhibited a complex shape. It is worth noting that the PL spectra of both SnO₂-NW/SiO₂/Si and δ -Ga₂O₃-NW/SiO₂/Si showed similarities, with vacancy-type defects being dominant in both cases. The I–V characteristics of SnO₂-NW/SiO₂/Si-n indicated near-metallic conductivity due to the presence of metallic tin. It should be noted that the deposition in SiO₂/Si-p templates was weak. This indicates that the filling efficiency or the density of the deposited material in the SiO₂/Si-p type templates was lower than expected, which might affect the quality and uniformity of the synthesized nanostructures. This observation suggests that further optimization of the deposition process may be required to achieve better filling and growth within these templates.

Author Contributions: Conceptualization, A.D. and A.I.P.; methodology, A.A. (Abdirash Akilbekov), J.K. and Z.B.; software, A.P. and Z.K.; validation, D.J., A.A. (Ainash Abdrakhmetova) and Z.B.; formal analysis, A.K.; investigation, A.K., D.J., A.A. (Ainash Abdrakhmetova), G.A., J.K. and Z.B.; data curation, A.A. (Abdirash Akilbekov); writing—original draft preparation, A.D. and D.J.; writing—review and editing, A.I.P.; visualization, G.A.; supervision, A.D.; project administration, A.A. (Abdirash Akilbekov); funding acquisition, A.D. All authors have read and agreed to the published version of the manuscript.

Funding: This research was funded by the Ministry of Science and Higher Education of the Republic of Kazakhstan, grant number AP14871479.

Data Availability Statement: The original contributions presented in this study are included in the article. Further inquiries can be directed to the corresponding author.

Acknowledgments: The work was carried out within the framework of the grant project AP14871479 of the Ministry of Science and Higher Education of the Republic of Kazakhstan.

Conflicts of Interest: The authors declare no conflicts of interest.

References

1. Lorenz, M.; Ramachandra Rao, M.S.; Venkatesan, T.; Fortunato, E.; Barquinha, P.; Branquinho, R. Topical Review: The oxide electronic materials and oxide interfaces roadmap. *J. Phys. D Appl. Phys.* **2016**, *49*, 433001. [\[CrossRef\]](#)
2. Varghese, B.; Hoong, T.C.; Yanwu, Z.; Reddy, M.V.; Chowdari, B.V.R.; Wee, A.T.S.; Vincent, T.B.C.; Lim, C.T.; Sow, C.H. Co₃O₄ nanostructures with different morphologies and their field-emission properties. *Adv. Funct. Mater.* **2007**, *17*, 1932–1939. [\[CrossRef\]](#)
3. Fang, X.S.; Yan, J.; Hu, L.F.; Liu, H.; Lee, P.S. Thin SnO₂ nanowires with uniform diameter as excellent field emitters: A stability of more than 2400 min. *Adv. Funct. Mater.* **2012**, *22*, 1613–1622. [\[CrossRef\]](#)
4. Bie, Y.Q.; Liao, Z.M.; Zhang, H.Z.; Li, G.R.; Ye, Y.; Zhou, Y.B.; Xu, J.; Qin, Z.X.; Dai, L.; Yu, D.P. Self-powered, ultrafast, visible-blind UV detection and optical logical operation based on ZnO/GaN nanoscale p-n junctions. *Adv. Funct. Mater.* **2011**, *23*, 649–653. [\[CrossRef\]](#)
5. Rigutti, L.; Tchernycheva, M.; Bugallo, A.D.; Jacopin, G.; Julien, F.H.; Zagonel, L.F.; March, K.; Stephan, O.; Kociak, M.; Songmuang, R. Ultraviolet photodetector based on GaN/AlN quantum discs in a single nanowire. *Nano Lett.* **2010**, *10*, 2939–2943. [\[CrossRef\]](#) [\[PubMed\]](#)
6. Tang, J.S.; Wang, C.Y.; Xiu, F.X.; Lang, M.R.; Chu, L.W.; Tsai, C.J.; Chueh, Y.L.; Chen, L.J.; Wang, K.L. Oxide-confined formation of germanium nanowire heterostructures for high-performance transistors. *Am. Chem. Soc. Nano* **2011**, *5*, 6008–6015. [\[CrossRef\]](#) [\[PubMed\]](#)
7. Kulmala, T.S.; Colli, A.; Fasoli, A.; Lombardo, A.; Haque, S.; Ferrari, A.C. Self-Aligned coupled nanowire. *Am. Chem. Soc. Nano* **2011**, *5*, 6910–6915. [\[CrossRef\]](#)
8. Kumar, S.; Tessarek, C.; Sarau, G.; Christiansen, S.; Singh, R. Self-Catalytic Growth of β -Ga₂O₃ Nanostructures by Chemical Vapor Deposition. *Adv. Eng. Mater.* **2015**, *17*, 709–715. [\[CrossRef\]](#)
9. Kumar, S.; Singh, R. Nanofunctional gallium oxide (Ga₂O₃) nanowires/nanostructures and their applications in nanodevices. *Phys. Status Solidi (RRL)—Rapid Res. Lett.* **2013**, *7*, 781–792. [\[CrossRef\]](#)
10. Murakami, H.; Nomura, K.; Goto, K.; Sasaki, K.; Kawara, K.; Thieu, Q.T.; Togashi, R.; Kumagai, Y.; Higashiwaki, M.; Kuramata, A.; et al. Homoepitaxial growth of β -Ga₂O₃ layers by halide vapor phase epitaxy. *Appl. Phys. Express* **2014**, *8*, 015503. [\[CrossRef\]](#)
11. Edwards, D.D.; Mason, T.O.; Goutenoire, F.; Poeppelmeier, K.R. A new transparent conducting oxide in the Ga₂O₃–In₂O₃–SnO₂ system. *Appl. Phys. Lett.* **1997**, *70*, 1706–1708. [\[CrossRef\]](#)
12. Shan, F.K.; Liu, G.X.; Lee, W.J.; Lee, G.H.; Kim, I.S.; Shin, B.C. Structural, electrical, and optical properties of transparent gallium oxide thin films grown by plasma-enhanced atomic layer deposition. *J. Appl. Phys.* **2005**, *98*, 023504. [\[CrossRef\]](#)
13. Ueda, N.; Hosono, H.; Waseda, R.; Kawazoe, H. Synthesis and control of conductivity of ultraviolet transmitting β -Ga₂O₃ single crystals. *Appl. Phys. Lett.* **1997**, *70*, 3561–3563. [\[CrossRef\]](#)
14. Matsuzaki, K.; Yanagi, H.; Kamiya, T.; Hiramatsu, H.; Nomura, K.; Hirano, M.; Hosono, H. Field-induced current modulation in epitaxial film of deep-ultraviolet transparent oxide semiconductor Ga₂O₃. *Appl. Phys. Lett.* **2006**, *88*, 092106. [\[CrossRef\]](#)
15. Fleischer, M.; Kornely, S.; Weh, T.; Frank, J.; Meixner, H. Selective gas detection with high-temperature operated metal oxides using catalytic filters. *Sens. Actuators B Chem.* **2000**, *69*, 205–210. [\[CrossRef\]](#)
16. Higashiwaki, M.; Sasaki, K.; Kuramata, A.; Masui, T.; Yamakoshi, S. Gallium oxide (Ga₂O₃) metal-semiconductor field-effect transistors on single-crystal β -Ga₂O₃ (010) substrates. *Appl. Phys. Lett.* **2012**, *100*, 013504. [\[CrossRef\]](#)
17. Higashiwaki, M.; Sasaki, K.; Kamimura, T.; Wong, M.H.; Krishnamurthy, D.; Kuramata, A.; Masui, T.; Yamakoshi, S. Depletion-mode Ga₂O₃ metal-oxide-semiconductor field-effect transistors on β -Ga₂O₃ (010) substrates and temperature dependence of their device characteristics. *Appl. Phys. Lett.* **2013**, *103*, 123511. [\[CrossRef\]](#)
18. Li, Y.; Tokizono, T.; Liao, M.; Zhong, M.; Koide, Y.; Yamada, I.; Delaunay, J.J. Efficient assembly of bridged β -Ga₂O₃ nanowires for solar-blind photodetection. *Adv. Funct. Mater.* **2010**, *20*, 3972–3978. [\[CrossRef\]](#)
19. Zou, R.; Zhang, Z.; Liu, Q.; Hu, J.; Sang, L.; Liao, M.; Zhang, W. High detectivity solar-blind high-temperature deep-ultraviolet photodetector based on multi-layered (100) facet-oriented β -Ga₂O₃ nanobelts. *Small* **2014**, *10*, 1848–1856. [\[CrossRef\]](#)
20. Feng, W.; Wang, X.; Zhang, J.; Wang, L.; Zheng, W.; Hu, P.; Cao, W.; Yang, B. Synthesis of two-dimensional β -Ga₂O₃ nanosheets for high-performance solar blind photodetectors. *J. Mater. Chem. C* **2014**, *2*, 3254–3259. [\[CrossRef\]](#)
21. Chang, P.C.; Fan, Z.; Tseng, W.Y.; Rajagopal, A.; Lu, J.G. β -Ga₂O₃ nanowires: Synthesis, characterization, and p-channel field-effect transistor. *Appl. Phys. Lett.* **2005**, *87*, 222102. [\[CrossRef\]](#)
22. Huang, Y.; Yue, S.; Wang, Z.; Wang, Q.; Shi, C.; Xu, Z.; Bai, X.D.; Tang, C.; Gu, C. Preparation and electrical properties of ultrafine Ga₂O₃ nanowires. *J. Phys. Chem. B* **2006**, *110*, 796–800. [\[CrossRef\]](#) [\[PubMed\]](#)
23. Hsieh, C.H.; Chou, L.J.; Lin, G.R.; Bando, Y.; Golberg, D. Nanophotonic switch: Gold-in-Ga₂O₃ peapod nanowires. *Nano Lett.* **2008**, *8*, 3081–3085. [\[CrossRef\]](#) [\[PubMed\]](#)
24. Tien, L.C.; Ho, C.H. Synthesis, optical characterization, and environmental applications of β -Ga₂O₃ nanowires. In *Gallium Oxide*; Pearton, S., Ren, F., Mastro, M., Eds.; Elsevier: Amsterdam, The Netherlands, 2019; pp. 67–90.

25. Dai, L.; Chen, X.L.; Zhang, X.N.; Jin, A.Z.; Zhou, T.; Hu, B.Q.; Zhang, Z.; Dai, L.; Chen, X.L.; Zhang, X.N.; et al. Growth and optical characterization of Ga₂O₃ nanobelts and nanosheets. *J. Appl. Phys.* **2002**, *92*, 1062–1064. [\[CrossRef\]](#)
26. Dai, Z.R.; Pan, Z.W.; Wang, Z.L. Novel nanostructures of functional oxides synthesized by thermal evaporation. *Adv. Funct. Mater.* **2003**, *13*, 9–24. [\[CrossRef\]](#)
27. Zhang, H.Z.; Kong, Y.; Wang, Y.; Du, X.; Bai, Z.; Wang, J.; Yu, D.; Ding, Y.; Hang, Q.; Feng, S. Ga₂O₃ nanowires prepared by physical evaporation. *Solid State Commun.* **1999**, *109*, 677–682. [\[CrossRef\]](#)
28. Liang, C.H.; Meng, G.W.; Wang, G.Z.; Wang, Y.W.; Zhang, L.D.; Zhang, S.Y. Catalytic synthesis and photoluminescence of β -Ga₂O₃ nanowires. *Appl. Phys. Lett.* **2001**, *78*, 3202–3204. [\[CrossRef\]](#)
29. Zhang, J.; Liu, Z.; Lin, C.; Lin, J. A simple method to synthesize β -Ga₂O₃ nanorods and their photoluminescence properties. *J. Cryst. Growth* **2005**, *280*, 99–106. [\[CrossRef\]](#)
30. Yu, M.F.; Atashbar, M.Z.; Chen, X. Mechanical and electrical characterization of β -Ga₂O₃/nanostructures for sensing applications. *IEEE Sens. J.* **2005**, *5*, 20–25. [\[CrossRef\]](#)
31. Gao, L.Y.; Zheng, M.J.; Zhong, M.; Li, M.; Ma, L. Preparation and photoinduced wettability conversion of superhydrophobic β -Ga₂O₃ nanowire film. *Appl. Phys. Lett.* **2007**, *91*, 013101. [\[CrossRef\]](#)
32. Periyasamy, M.; Kar, A. Modulating the properties of SnO₂ nanocrystals: Morphological effects on structural, photoluminescence, photocatalytic, electrochemical and gas sensing properties. *J. Mater. Chem.* **2020**, *8*, 4604–4635. [\[CrossRef\]](#)
33. Shi, H.; Cheng, B.; Cai, Q.; Su, X.; Xiao, Y.; Lei, S. Surface state controlled ultrahigh selectivity and sensitivity for UV photodetectors based on individual SnO₂ nanowires. *J. Mater. Chem.* **2016**, *4*, 8399–8406. [\[CrossRef\]](#)
34. Li, Y.; Valle, F.D.; Simonnet, M.; Yamada, I.; Delaunay, J. High-performance UV detector made of ultra-long ZnO bridging nanowires. *Nanotechnology* **2009**, *20*, 045501. [\[CrossRef\]](#) [\[PubMed\]](#)
35. Jiang, J.; Heck, F.; Hofmann, D.M.; Eickhoff, M. Synthesis of SnO₂ Nanowires Using SnI₂ as Precursor and Their Application as High-Performance Self-Powered Ultraviolet Photodetectors. *Phys. Status Solidi B* **2018**, *255*, 1700426. [\[CrossRef\]](#)
36. Luo, L.; Liang, F.; Jie, J. Sn-catalyzed synthesis of SnO₂ nanowires and their optoelectronic characteristics. *Nanotechnology* **2011**, *22*, 485701–485708. [\[CrossRef\]](#)
37. Wu, J.M.; Kuo, C.H. Ultraviolet photodetectors made from SnO₂ nanowires. *Thin Solid Film.* **2009**, *517*, 3870–3873. [\[CrossRef\]](#)
38. Jones, M.R.; Osberg, K.D.; MacFarlane, R.J.; Langille, M.R.; Mirkin, C.A. Templated techniques for the synthesis and assembly of plasmonic nanostructures. *Chem. Rev.* **2011**, *111*, 3736–3827. [\[CrossRef\]](#) [\[PubMed\]](#)
39. Routkevitch, D.; Bigioni, T.; Moskovits, M.; Xu, J.M. Electrochemical fabrication of CdS nanowire arrays in porous anodic aluminum oxide templates. *J. Phys. Chem.* **1996**, *100*, 14037–14047. [\[CrossRef\]](#)
40. Zhang, F.; Zhao, D. Fabrication of ordered magnetite-doped rare earth fluoride nanotube arrays by nanocrystal self-assembly. *Nano Res.* **2009**, *2*, 292–305. [\[CrossRef\]](#)
41. Kenzhina, I.E.; Zdorovets, M.V.; Kozlovskiy, A.L.; Kadyrzhanov, K.K. Synthesis and properties of Cu/CuO nanostructures obtained by electrochemical deposition. *Mater. Res. Express* **2018**, *3*, 035052. [\[CrossRef\]](#)
42. Kozlovskii, A.L.; Kadyrzhanov, K.K.; Zdorovets, M.V. Structural and Conductive Characteristics of Fe/Co Nanotubes. *Russ. J. Electrochem.* **2018**, *54*, 178–185. [\[CrossRef\]](#)
43. Kadyrzhanov, K.K.; Kozlovskiy, A.L.; Kanyukov, E.Y.; Mashentseva, A.A.; Zdorovets, M.V.; Shumskaya, A.E. Variation of polymer-template pore geometry as a means of controlling the magnetic properties of metallic nanostructures. *Pet. Chem.* **2017**, *57*, 790–795. [\[CrossRef\]](#)
44. Mashentseva, A.A.; Ibragimova, M.A.; Akhmetova, S.B.; Kozlovskiy, A.L.; Zdorovets, M.V.; Amirkhanova, Z.T. Synthesis, radical scavenging, and antimicrobial activities of core-shell Au/Ni microtubes. *Chem. Pap.* **2020**, *74*, 2189–2199. [\[CrossRef\]](#)
45. Dauletbekova, A.; Akyzbekova, A.; Sarsekhan, G.; Usseinov, A.; Baimukhanov, Z.; Kozlovskiy, A.; Vlasukova, L.A.; Komarov, F.F.; Popov, A.I.; Akilbekov, A.T. Ion-Track Template Synthesis and Characterization of ZnSeO₃ Nanocrystals. *Crystals* **2022**, *12*, 817. [\[CrossRef\]](#)
46. Akyzbekova, A.; Dauletbekova, A.; Baymukhanov, Z.; Kozlovsky, A.; Usseinov, A. ZnSe₂O₅ nanocrystals synthesis in a nanoporous layer of silicon dioxide on silicon In Proceedings of the 6th International Young Researchers' Conference on Physics, Technologies and Innovation, PTI 2019, Ekaterinburg, Russia, 20–23 May 2019.
47. Vlasukova, L.A.; Komarov, F.F.; Yuvchenko, V.N.; Wesch, W.; Wendler, E.; Didyk, A.Y.; Skuratov, V.A.; Kislitsin, S.B. Threshold and criterion for ion track etching in SiO₂ layers grown on Si. *Vacuum* **2014**, *105*, 107–110. [\[CrossRef\]](#)
48. Akyzbekova, A.; Dauletbekova, A.; Baimukhanov, Z.; Vlasukova, L.A.; Usseinov, A.; Saduova, N.; Akilbekov, A.T.; Pankratov, V.A.; Popov, A.I. Annealing Effect on Structural, Optical and Electrophysical Properties of ZnSe Nanocrystals Synthesized into SiO₂/Si Ion Track Template. *Materials* **2024**, *17*, 4149. [\[CrossRef\]](#)
49. Aralbayeva, G.; Sarsekhan, G.; Akyzbekova, A.; Vlasukova, L.A.; Baimukhanov, Z.; Yuvchenko, V.; Bazarbek, A.-D.; Dauletbekova, A.; Kabdrakhimova, G.; Akilbekov, A.T. The Thermal Stability and Photoluminescence of ZnSeO₃ Nanocrystals Chemically Synthesized into SiO₂/Si Track Templates. *Crystals* **2024**, *14*, 730. [\[CrossRef\]](#)
50. Vlasukova, L.; Komarov, F.; Yuvchenko, V.; Baran, L.; Milchanin, O.; Dauletbekova, A.; Alzhanova, A.; Akilbekov, A. Etching of latent tracks in amorphous SiO₂ and Si₃N₄: Simulation and experiment. *Vacuum* **2016**, *29*, 137. [\[CrossRef\]](#)
51. Ziegler, J.F.; Biersack, J.P.; Ziegler, M.D. SRIM. The Stopping and Range of Ions in Matter. In *Treatise on Heavy-Ion Science*; Springer: Boston, MA, USA, 1985; Volume 278. [\[CrossRef\]](#)

52. Kaniukov, E.Y.; Ustarroz, J.; Yakimchuk, D.V.; Petrova, M.; Terryn, H.; Sivakov, V.; Petrov, A.V. Tunable nanoporous silicon oxide templates by swift heavy ion tracks technology. *Nanotechnology* **2016**, *27*, 115305. [\[CrossRef\]](#)
53. Roy, R.; Hill, V.G.; Osborn, E.F. Polymorphism of Ga₂O₃ and the system Ga₂O₃—H₂O. *J. Am. Chem. Soc.* **1952**, *74*, 719–722. [\[CrossRef\]](#)
54. Yoshioka, S.; Hayashi, H.; Kuwabara, A.; Oba, F.; Matsunaga, K.; Tanaka, I. Structures and energetics of Ga₂O₃ polymorphs. *J. Phys. Condens. Matter* **2007**, *19*, 346211. [\[CrossRef\]](#)
55. Erba, A.; Desmarais, J.K.; Casassa, S.; Civalleri, B.; Donà, L.; Bush, I.J.; Searle, B.; Maschio, L.; Edith-Daga, L.; Cossard, A.; et al. CRYSTAL23: A program for computational solid state physics and chemistry. *J. Chem. Theory Comput.* **2022**, *19*, 6891–6932. [\[CrossRef\]](#)
56. Adamo, C.; Barone, V. Toward reliable density functional methods without adjustable parameters: The PBE0 model. *J. Chem. Phys.* **1999**, *110*, 6158–6170. [\[CrossRef\]](#)
57. Ernzerhof, M.; Scuseria, G.E. Assessment of the Perdew–Burke–Ernzerhof exchange–correlation functional. *J. Chem. Phys.* **1999**, *110*, 5029–5036. [\[CrossRef\]](#)
58. Vilela Oliveira, D.; Laun, J.; Peintinger, M.F.; Bredow, T. BSSE-correction scheme for consistent gaussian basis sets of double-and triple-zeta valence with polarization quality for solid-state calculations. *J. Comput. Chem.* **2019**, *40*, 2364–2376. [\[CrossRef\]](#) [\[PubMed\]](#)
59. Baimukhanov, Z.; Dauletbekova, A.; Junisbekova, D.; Kalytko, V.; Akilbekov, A.; Akylbekova, A.; Baubekova, G.; Aralbayeva, G.; Bazarbek, A.-D.; Usseinov, A.; et al. Synthesis of Orthorhombic Tin Dioxide Nanowires in Track Templates. *Materials* **2024**, *17*, 1226. [\[CrossRef\]](#)
60. He, H.; Orlando, R.; Blanco, M.A.; Pandey, R.; Amzallag, E.; Baraille, I.; Rérat, M. First-principles study of the structural, electronic, and optical properties of Ga₂O₃ in its monoclinic and hexagonal phases. *Phys. Rev. B Condens. Matter Mater. Phys.* **2006**, *74*, 195123. [\[CrossRef\]](#)
61. Varley, J.B.; Weber, J.R.; Janotti, A.; Van De Walle, C.G. Oxygen vacancies and donor impurities in β-Ga₂O₃. *Appl. Phys. Lett.* **2010**, *97*, 142106. [\[CrossRef\]](#)
62. Peelaers, H.; Van de Walle, C.G. Brillouin zone and band structure of β-Ga₂O₃. *Phys. Status Solidi* **2015**, *252*, 828–832. [\[CrossRef\]](#)
63. Harwig, T.; Kellendonk, F.; Slappendel, S. The ultraviolet luminescence of β-galliumsesquioxide. *J. Phys. Chem. Solids* **1978**, *39*, 675–680. [\[CrossRef\]](#)
64. Blasse, G.; Bril, A. Some observations on the luminescence of β-Ga₂O₃. *J. Phys. Chem. Solids* **1970**, *31*, 707–711. [\[CrossRef\]](#)
65. Harwig, T.; Kellendonk, F. Some observations on the photoluminescence of doped β-galliumsesquioxide. *J. Solid-State Chem.* **1978**, *24*, 255–263. [\[CrossRef\]](#)
66. Villora, E.G.; Hatanaka, K.; Odaka, H.; Sugawara, T.; Miura, T.; Fukumura, H.; Fukuda, T. Luminescence of undoped β-Ga₂O₃ single crystals excited by picosecond X-ray and sub-picosecond UV pulses. *Solid State Commun.* **2003**, *127*, 385–388. [\[CrossRef\]](#)
67. Zhou, X.T.; Heigl, F.; Ko, J.Y.P.; Murphy, M.W.; Zhou, J.G.; Regier, T.; Blyth, R.I.R.; Sham, T.K. Origin of luminescence from Ga₂O₃ nanostructures studied using x-ray absorption and luminescence spectroscopy. *Phys. Rev. B—Condens. Matter Mater. Phys.* **2007**, *75*, 125303. [\[CrossRef\]](#)
68. Guzman-Navarro, G.; Herrera-Zaldivar, M.; ValenzuelaBenavides, J.; Maestre, D. CL study of blue and UV emissions in β-Ga₂O₃ nanowires grown by thermal evaporation of GaN. *J. Appl. Phys.* **2011**, *110*, 034315. [\[CrossRef\]](#)
69. Lopez, I.; Utrilla, A.D.; Nogales, E.; Mendez, B.; Piqueras, J.; Peche, A.; Ramirez-Castellanos, J.; GonzalezCalbet, J.M. In-doped gallium oxide micro-and nanostructures: Morphology, structure, and luminescence properties. *J. Phys. Chem. C* **2012**, *116*, 3935–3943. [\[CrossRef\]](#)
70. Varley, J.B.; Janotti, A.; Franchini, C.; Van De Walle, C.G. Role of self-trapping in luminescence and p-type conductivity of wide-band-gap oxides. *Phys. Rev. B—Condens. Matter Mater. Phys.* **2012**, *85*, 081109. [\[CrossRef\]](#)
71. Villora, E.G.; Yamaga, M.; Inoue, T.; Yabasi, S.; Mausi, Y.; Sugawara, T.; Fukuda, T. Optical spectroscopy study on β-Ga₂O₃. *Jpn. J. Appl. Phys.* **2002**, *41*, L622. [\[CrossRef\]](#)
72. Yamahara, H.; Seki, M.; Tabata, H. Growth of gallium oxide nanowires by pulsed laser deposition. *J. Cryst. Process Technol.* **2012**, *2*, 125–129. [\[CrossRef\]](#)
73. Munnix, S.; Schmeits, M. Electronic structure of tin dioxide surfaces. *Phys. Rev. B* **1983**, *27*, 7624. [\[CrossRef\]](#)
74. Chiodini, N.; Paleari, A.; DiMartino, D.; Spinolo, G. SnO₂ nanocrystals in SiO₂: A wide-band-gap quantum-dot system. *Appl. Phys. Lett.* **2002**, *81*, 1702–1704. [\[CrossRef\]](#)
75. Vanheusden, K.; Warren, W.L.; Seager, C.H.; Tallant, D.R.; Voigt, J.A.; Gnade, B.E. Mechanisms behind green photoluminescence in ZnO phosphor powders. *J. Appl. Phys.* **1996**, *79*, 7983–7990. [\[CrossRef\]](#)
76. Liu, Y.; Yang, Q.; Xu, C. Single-narrow-band red upconversion fluorescence of ZnO nanocrystals codoped with Er and Yb and its achieving mechanism. *J. Appl. Phys.* **2008**, *104*, 064701. [\[CrossRef\]](#)
77. Godinho, K.G.; Walsh, A.; Watson, G.W. Energetic and electronic structure analysis of intrinsic defects in SnO₂. *J. Phys. Chem. C* **2009**, *113*, 439–448. [\[CrossRef\]](#)
78. Her, Y.C.; Wu, J.Y.; Lin, Y.R.; Tsai, S.Y. Low-temperature growth and blue luminescence of SnO₂ nanoblades. *Appl. Phys. Lett.* **2006**, *89*, 043115. [\[CrossRef\]](#)
79. Rani, S.; Roy, S.; Karar, N.; Bhatnagar, M. Structure, microstructure and photoluminescence properties of Fe doped SnO₂ thin films. *Solid State Commun.* **2007**, *141*, 214–218. [\[CrossRef\]](#)

80. Bhatnagar, M.; Kaushik, V.; Kaushal, A.; Singh, M.; Mehta, B. Structural and photoluminescence properties of tin oxide and tin oxide: C core-shell and alloy nanoparticles synthesised using gas phase technique. *AIP Adv.* **2016**, *6*, 095321. [[CrossRef](#)]
81. Duan, J.; Gong, J.; Huang, H.; Zhao, X.; Cheng, G.; Yu, Z.; Yang, S. Multiform structures of SnO₂ nanobelts. *Nanotechnology* **2007**, *18*, 055607. [[CrossRef](#)]
82. Zhang, L.; Ge, S.; Zuo, Y.; Zhang, B.; Xi, L. Influence of oxygen flow rate on the morphology and magnetism of SnO₂ nanostructures. *J. Phys. Chem. C* **2010**, *114*, 7541–7547. [[CrossRef](#)]
83. Hu, J.Q.; Bando, Y.; Liu, Q.L.; Golberg, D. Laser-ablation growth and optical properties of wide and long single-crystal SnO₂ ribbons. *Adv. Funct. Mater.* **2003**, *13*, 493–496. [[CrossRef](#)]
84. Cheng, B.; Russell, J.M.; Shi Zhang, L.; Samulski, E.T. Large-scale, solution-phase growth of single-crystalline SnO₂ nanorods. *J. Am. Chem. Soc.* **2004**, *126*, 5972–5973. [[CrossRef](#)]
85. Tousekova, J.; Tousek, J.; Klier, E.; Kuzel, R. Preparation and basic electrical properties of CdTe thick films. *Phys. Status Solidi* **1979**, *56*, 315–322. [[CrossRef](#)]
86. Davis, E.A. States in the gap and defects in amorphous semiconductors. *Amorph. Semicond.* **2005**, *36*, 41–72.

Disclaimer/Publisher's Note: The statements, opinions and data contained in all publications are solely those of the individual author(s) and contributor(s) and not of MDPI and/or the editor(s). MDPI and/or the editor(s) disclaim responsibility for any injury to people or property resulting from any ideas, methods, instructions or products referred to in the content.